

1. INTRODUCTION

Experimental and computational investigations of the dynamic stall phenomenon continue to attract the attention of various research groups in the major aeronautical research laboratories. There are two reasons for this continued research interest. First, the occurrence of dynamic stall on the retreating blade of helicopters imposes a severe performance limitation and thus suggests to search for ways to delay the onset of dynamic stall. Second, the lift enhancement prior to dynamic stall presents an opportunity to achieve enhanced maneuverability of fighter aircraft. A description of the major parameters affecting dynamic stall and lift and an evaluation of research efforts prior to 1988 has been given by Carr [1].

Unfortunately, the basic fluid physics underlying the dynamic stall phenomenon is still far from being fully understood. This is due to the difficulty of making sufficiently detailed measurements on fast moving airfoils so that the processes leading to unsteady flow separation, vortex formation/propagation, and unsteady flow reattachment can be identified. These processes are further complicated by the possibility of shock formation and unsteady shock/boundary layer interaction as the free-stream Mach number is increased. The development of reliable computational prediction methods, in turn, is dependent on the availability of sufficiently detailed flow information about the dynamic stall processes.

In this paper the authors' recent progress in the development of experimental and computational methods to analyze the dynamic stall phenomena occurring on NACA 0012 airfoils is reviewed. First, the major experimental and computational approaches and results are summarized. This is followed by an assessment of our results and an outlook toward the future.

2. EXPERIMENTAL PROGRESS

In this section we summarize the experimental results obtained in the Compressible Dynamic Stall Facility of the NASA Ames Fluid Mechanics Laboratory since our last review [2]. Additional details

about this facility and the experimental techniques used in these experiments can be found in references [3-9]. All the measurements described in this section were obtained on a NACA 0012 airfoil of 7.62 cm (3 inch) chord subjected to sinusoidal pitch oscillations about the quarter-chord point or to a ramp-change in angle of attack. The maximum frequency achieved was 100 Hz, the maximum pitch rate 3600 degrees per second. The Reynolds number ranged between 200,000 to 900,000. Further details can be found in the cited references.

2.1 Effect of Mach Number and Pitch Rate on Dynamic Stall

A series of experiments was performed to determine the effect of Mach number and pitch rate on the dynamic stall initiation and evolution. To this end stroboscopic schlieren pictures were taken over a Mach number range from 0.2 to 0.45, a non-dimensional pitch rate range from 0.02 to 0.05 for airfoils undergoing a ramp change in angle of attack, and a reduced frequency range of 0.025 to 0.1 for airfoils in sinusoidal pitch motion. The non-dimensional pitch rate is defined as the pitch rate (radians/sec) \times chord / free-stream speed. The reduced frequency is defined as frequency of oscillation (Hz) \times pi \times chord / free-stream speed.

Figure 1 shows the observed vortex release angles for ramp and sinusoidal motions as a function of Mach number and pitch rate or reduced frequency. The following trends are clearly discernible:

- an increase in reduced frequency delays the onset of dynamic stall to higher angles of attack
- at free-stream Mach numbers greater than 0.3 compressibility effects are significant, producing drastically reduced stall onset angles of attack.

2.2 Visualization of Leading-Edge Details

Using the stroboscopic schlieren technique [3] locally supersonic flow near the leading edge could be successfully identified in a number of cases. For example, Figure 2 shows the leading edge flow details for a free-stream Mach number of 0.45 as the airfoil is pitching upwards at a non-dimensional pitch rate of 0.0313 through an angle of attack of 12.6 degrees. Several discontinuities are clearly visible within the first 5 - 8% chord distance. At this Mach number locally supersonic flow is reached (verified by interferometry). Therefore these discontinuities most likely are caused by the formation of weak multiple shocks due to the recompression and the interaction with the boundary layer.

* Navy-NASA Joint Institute of Aeronautics
Naval Postgraduate School, Monterey, CA

U.S. Army Aeroflightdynamics Directorate
and Fluid Dynamics Research Branch
NASA Ames Research Center
Moffett Field, California

Eventually, these weak interactions are followed by a stronger shock which recompresses the flow to subsonic values. Similar stroboscopic schlieren pictures were obtained over a range of angles of attack from 12.2 to 12.9 degrees for the same free-stream Mach number and pitch rate.

Another interesting observation is the formation of multiple vortices under certain circumstances rather than the roll-up into a single dynamic stall vortex. Figure 3 presents an enlarged schlieren picture for a free-stream Mach number of 0.25, as the airfoil pitches at a pitch rate of 0.025 through an angle of attack of 16.5 degrees. Two clockwise vortical structures can be identified. Multiple vortices were observed only at low pitch rates and low Mach numbers, whereas at higher Mach numbers a single dynamic stall vortex was seen to form.

2.3 Quantitative Measurements of Dynamic Stall Onset

A more quantitative determination of the leading edge flow details and therefore of the dynamic stall onset mechanism is made possible by means of point diffraction interferometry [6]. Typical interferograms obtained with this technique are shown in Figures 4 for the NACA 0012 airfoil oscillating at a reduced frequency of 0.05 in a $M=0.33$ flow. In these interferograms the fringes (the alternating dark and light lines in the photographs) denote lines of constant Mach number [7]. In Figure 4a, the flow over the airfoil at an angle below stall is presented for an angle of 10 degrees. Note the fringes which leave the leading edge turn parallel to the surface, and then abruptly turn toward the surface of the airfoil once more. As explained in [6], this pattern is indicative of a laminar separation bubble. In contrast, Figure 4b shows the onset of dynamic stall as the airfoil oscillates through an angle of attack of 13.6 degrees. The fringes no longer rapidly curve back to the surface near the leading edge. Instead, they are displaced aft until, further downstream, they again turn normal to the surface, denoting the development of a dynamic stall vortex. Furthermore, the fringe patterns indicate that the dynamic stall develops from a region of strong gradients which encloses a low energy region, in contrast to the symmetric density field one would expect from a classical vortex.

Further quantification of the flow field around the leading edge is made possible by digital processing of the interferograms [7]. Using a specially designed, screen-oriented digitizing program fringe contour maps, as shown in Figure 5, could be obtained. As noted above each fringe is a line of constant density, and thus also of constant Mach number. Therefore, the fringe maps can be used to quantify the effect of unsteadiness on the local pressure distributions. Figure 5 shows

the fringe pattern differences near the leading edge of the NACA 0012 airfoil in a $M=0.33$ flow at a steady 10 degrees angle of attack versus the case of oscillation at $k=0.1$ when the airfoil passes through the same angle of attack. It can be seen that a separation bubble starts to develop in the steady case while no such development occurs as yet in the oscillating case. Figure 6 shows a plot of the suction peaks determined from the fringe maps [7] for several Mach numbers and reduced frequencies. It is seen that a maximum suction pressure coefficient of -4.96 is reached at $M=0.3$ (corresponding to a Reynolds number of 540,000) for three different values of reduced frequency $k=0.05, 0.075$ and 0.10 , thus suggesting that stall develops once the suction pressure reaches a maximum value, independent of reduced frequency. This value is reached at progressively higher angles of attack with increasing frequency. Figure 7 shows the leading edge pressure distributions inferred from the fringe patterns as a function of reduced frequency. Again, it can be seen that the development of leading edge pressure gradients is delayed due to the airfoil oscillation. This supports the suggestion that stall delay is brought about by the lag in pressure build-up due to inviscid unsteady flow effects. It remains to be seen whether this is the dominant effect. This point will be addressed further in section 3.2. Furthermore, it is noteworthy to observe from Figure 6 that the maximum suction pressure coefficient decreases as the Mach number is increased.

Additional flow field information about the dynamic stall onset mechanism was obtained by means of laser-doppler velocimetry [8]. Figure 8 shows the distribution of the axial and normal components of the velocity vectors in the separation bubble which has formed on the NACA 0012 airfoil as it oscillates in a $M=0.3$ flow at a reduced frequency of $k=0.05$ with an amplitude of 10 degrees about a mean angle of 10 degrees. The measuring station is at $x/c=0.083$, that is very close to the leading edge. The measured velocity profiles are plotted as a function of phase angle, such that a phase angle of 90 degrees corresponds to zero angle of attack, 180 degrees to 10 degrees angle of attack during the upstroke and so on. It is seen that at a phase angle of 160 degrees, corresponding to 6 degrees incidence on the upstroke, there is a rapid drop in the u-velocity component close to the airfoil surface at $y/c=0.067$ from values significantly greater than the free-stream speed to values somewhat below the free-stream speed. Hence no flow reversal is observed yet at this measuring station although reverse flow can be expected very close to the wall. Unfortunately, no measurements could be taken closer to the wall due to the laser beam configuration used. The v-component of the velocity vector remains constant until a phase angle of 186 degrees is reached corresponding to an angle of attack slightly less than 11 degrees. At a phase angle of

about 200 degrees, (13.4 degrees incidence), an abrupt increase in the v-component develops near the leading edge which appears to be caused by the break-up of the separation bubble. Very closely spaced additional measurements [8] showed that the bubble extends from $0.017 < x/c < 0.167$ along the surface and reaches out to about 15% chord.

Further LDV mapping of the flow field at additional measuring stations revealed that during the initial part of the upstroke the flow experiences rapid accelerations over a large region of the airfoil reaching instantaneous values 80% higher than the free-stream value. The corresponding PDI images confirmed the presence of these large velocities outside of the separation bubble, extending over a significant distance normal to the wall as well as downstream from the leading-edge. As the airfoil angle of attack starts to exceed the static stall angle a wake-like profile develops near the wall as a result of bubble breakdown.

2.4 Quantitative Measurements of the Reattachment Mechanism

The previously described three experimental techniques, schlieren visualization, point diffraction interferometry, and laser-doppler velocimetry, were also used to identify the detailed flow reattachment process during the downstroke [9]. The flow condition was again $M=0.3$, corresponding to a Reynolds number of 540,000. The airfoil again oscillated about a mean angle of 10 degrees with an amplitude of 10 degrees.

First, schlieren visualization identified the steady stall angle to be 12.33 degrees, with no measurable hysteresis effect. In contrast, schlieren visualization of the flow over the oscillating airfoil revealed that flow reattachment after dynamic stall is a continuous process which extends over a significant range of angles of attack (from about 14 degrees down to about 6 degrees in this particular case). At 13.82 degrees on the downstroke, the flow begins to reattach around the leading-edge while the remainder of the upper surface flow is still separated. At 10 degrees, reattachment has progressed to about 10% chord from the leading-edge. A further decrease in angle of attack leads to a further downstream progression of the reattachment while a separation bubble starts to form near the leading-edge. A further decrease in angle of attack tends to shrink the separation bubble which finally vanishes at about 6 degrees. This sequence of events is shown schematically in Figure 9. Additional point diffraction and LDV measurements lend further support to this scenario of evolution of the reattachment process. Figure 10 shows the maximum suction pressure history during the downstroke. As reattachment progresses, the leading-edge

suction increases with decreasing angle of attack, down to about 8 degrees incidence. Near the steady stall angle the suction reaches a plateau which is indicative of the bubble formation. This evolution of the pressure distributions during the downstroke is shown more clearly in Figure 11. The measured velocity profiles near the leading-edge at station $x/c=0.083$ at 10 degrees and 5.46 degrees during the up and downstroke are shown in Figure 12. The large hysteresis effect can clearly be seen at 10 degrees while at 5.46 degrees the flow is fully attached and hence no hysteresis is present any longer.

3. COMPUTATIONAL PROGRESS

In this section we summarize the computational results obtained since our last review. Additional details can be found in references 10 and 11.

3.1 Numerical Solution of the Navier-Stokes Equations

The thin-layer approximation of the Navier-Stokes equations in conservation law form, written for an inertial reference frame, was used. All quantities were discretized at every node using finite differences. The physical space points were mapped to the computational domain points by means of a generalized coordinate transformation. For the time integration the implicit trapezoidal rule was used. After linearization and space discretization the space integration was performed with the Beam-Warming, factorized, iterative algorithm. A Jameson-type blended second and fourth-order dissipation term based on the computed pressure field was incorporated to suppress high-frequency numerical oscillations and to enable capturing of shocks. For subsonic shock-free solutions only the fourth-order dissipation was used. In addition, an implicit fourth-order smoothing was used on the left side of the equations for numerical stability. Both the implicit and explicit dissipation were scaled by the spectral radius and with the time step. The latter scaling makes the steady-state solution independent of time step. Since the added dissipation terms modify the original partial differential equation the dissipation coefficients were kept as small as possible for unsteady computation. Elimination of the error introduced by the linearization and approximate factorization may be accomplished by performing Newton subiterations to convergence within each time step.

The boundary conditions were specified as follows. At the outer boundaries zero-order Riemann invariant extrapolation was used. On the airfoil surface the non-slip condition was applied for the velocities, and the density and pressure were obtained from the interior by simple extrapolation. For

the C-type grids used in this investigation averaging of the flow variables across the wake-cut was incorporated.

Fully turbulent flow calculations only were performed by implementing three different turbulence models into the above-described numerical code. These were the Baldwin-Lomax and the RNG algebraic eddy viscosity models and the one-equation Johnson-King model. For a more detailed description of these models we refer to [11] and to the original references contained therein.

3.2 Computation of Dynamic Stall Onset

A series of calculations was performed with the above described Navier-Stokes code in combination with the Baldwin-Lomax turbulence model to investigate the evolution of dynamic stall in response to a ramp-change in angle of attack of a NACA 0012 airfoil. The Reynolds number was chosen to be sufficiently high so that fully turbulent flow could be assumed. Figure 13 shows the computed flow field as the airfoil pitches through an angle of attack of 17 degrees in a $M=0.4$ and $Re=4,000,000$ flow. It can be seen that the flow separates near the leading-edge but reattaches again further downstream thus forming a recirculatory flow region. Another recirculatory flow region then forms near the trailing-edges. A further increase in angle of attack produces a rapid growth and a merging of the two recirculatory flow regions and the formation of the dynamic stall vortex. A more detailed study of the effect of pitch rate and of Mach number on the onset of flow reversal near the leading edge of the NACA 0012 airfoil and of two modified NACA 0012 airfoils [10] showed that the onset of flow reversal follows the same trends as observed in the experiments. An increase in Mach number shifts the flow reversal to lower angles of attack, whereas an increase in pitch rate delays the flow reversal to higher angles of attack. More specifically, as shown in Figure 14, the onset of flow reversal appears to occur in response to substantially the same critical pressure gradient distribution. The delay to higher pitch rate therefore appears to be due primarily to the lag in inviscid pressure build-up.

3.3 Computation of the Reattachment Mechanism during Light Stall

Further details of the flow behavior were also computed for small amplitude sinusoidal pitch oscillations near static stall [11]. Figures 15 and 16 show a flow field comparison as the airfoil oscillates through 14.7 degrees during the up and downstroke for a pitch oscillation about the quarter chord point in a free-stream flow of $M=0.3$ at a Reynolds number of 2 million. The airfoil oscillates with an amplitude of 2.5 degrees about a mean angle of 13 degrees.

This corresponds to the case of light stall because the static stall angle of approximately 13.5 degrees is slightly exceeded during part of the oscillation. As shown experimentally by Carta and Lorber [12], the light stall regime is prone to lead to stall flutter. Hence, there is considerable interest to develop computational procedures to predict this phenomenon. It is seen from Figures 15 and 16 that there is a substantial thickening of the boundary layer during the downstroke and that the computed flow field (in terms of instantaneous particle traces) is quite different during the up and downstroke at 14.7 degrees. As soon as the static stall angle is exceeded a reversed flow region forms near the trailing-edge during the upstroke. It continues to grow to its maximum value at an angle of attack of 15.3 degrees during the downstroke and then diminishes again until the flow is fully reattached at around 12 degrees. The flow field differences during the up and downstroke produce the well known lift and moment hysteresis effects. In Figure 17 the computed moment hysteresis loops are compared with the measured moment loops [11]. In this case the oscillation amplitude was 5.5 degrees about a mean angle of 10 degrees at a Mach number of 0.3, a Reynolds number of 4 million, and a reduced frequency of 0.1. The experimental curves resemble a figure eight. Instability occurs as soon as the area enclosed by the clockwise part of the loop exceeds the counterclockwise area. The computed loops are purely counterclockwise loops and hence fail to predict the onset of stall flutter. This failure can be traced to the Navier-Stokes code's inability to predict the measured collapse of the suction peak shown in Figure 18. The computed pressure distributions only indicate the formation of a recirculatory flow region near the trailing-edge. Additional calculations using the Johnson-King and the RNG turbulence model rather than the Baldwin-Lomax model produced significantly different recirculatory flow regions and hence hysteresis loops, but none were able to predict the experimental distributions [11].

4. DISCUSSION

For the analysis of the above experimental and computational results it appears to be useful to consider the characteristic response times which are likely to affect the flow phenomena. Introducing the aerodynamic time as the proper reference unit, i.e., the time it takes a free-stream particle to travel one chord length, the aerodynamic times used in the above described experiments varied from 0.00115 sec at $M=0.2$ to 0.0005 sec at $M=0.45$ (for the NACA 0012 airfoil of 7.62 cm chord). The ramp rise times to the maximum lift (at about 17 degrees incidence) used in these experiments varied from about 0.0125 sec at $M=0.2$ to 0.005 sec at $M=0.45$, corresponding to about 10 aerodynamic time

units. Wagner's lift response to a step change in angle of attack indicates that it takes about 50 aerodynamic times to reach the steady-state lift value. Since the ramp rise time to maximum lift is significantly shorter than the time to reach steady-state lift significant inviscid unsteady aerodynamic effects (delays) can be expected to occur. On the other hand, the step response of the boundary layer typically is of the order of the aerodynamic time, as discussed for example by Hancock and Mabey [13]. Therefore it can be expected that the observed and computed stall onset delays are caused primarily by the lag in the inviscid pressure build-up. Since the boundary layer responds almost instantaneously to the imposed pressure the flow reversal and stall onset will occur as soon as a certain critical pressure level or pressure gradient distribution has been reached (see sections 2.3 and 3.2).

Although the Navier-Stokes computations appear to be capable of predicting the stall onset delay due to increasing pitch rate several serious deficiencies are apparent. One concerns the need for a greatly improved resolution and computation of the boundary layer region. A second deficiency concerns the inability to include the boundary layer transition phenomenon. Although recirculation regions can be obtained with a fully turbulent Navier-Stokes code (as shown in Figure 11) the realism of such computations is questionable. The importance of proper transition modelling has been shown in viscous-inviscid interaction calculations [14,15], especially for airfoil flows at Reynolds numbers less than one million. Therefore transition modelling will have to be incorporated into the present Navier-Stokes code if the separation bubbles described in section 2.2 for Reynolds numbers ranging from 200,000 to 900,000 are to be modelled successfully. A further uncertainty concerns the effect of flow unsteadiness on the transition process. Since no experimental data are available such modelling will have to be based on steady-state information only. Finally, the inability of the commonly used turbulence models (Baldwin-Lomax, Johnson-King, RNG) to predict the reattachment process (see section 3.3) is a further obstacle to the successful computation of dynamic stall phenomena.

It is likely that certain aspects of the dynamic stall phenomenon, such as the dynamic stall onset, can be modelled more efficiently and successfully with viscous-inviscid interaction approaches rather than with numerical solutions of the Navier-Stokes equations. Viscous-inviscid interaction procedures permit the efficient computation of detailed boundary layer information and the incorporation of transition modelling by either using empirical transition onset models or stability calculations and empirical transition length models. Cebeci et al [16,17] recently extended steady viscous-

inviscid airfoil computations to airfoils undergoing ramp-type and sinusoidal oscillations. Results obtained for a Sikorsky airfoil appear sufficiently encouraging to further develop this method and to apply it to the NACA 0012 measurements described in section 2.

SUMMARY and OUTLOOK

Experimental and computational investigations of the dynamic airfoil stall phenomena occurring on NACA 0012 airfoils subjected to harmonic time oscillations or to ramp-type changes in angle of attack have been described. Using optical interference-free flow visualization and flow-measuring techniques, such as stroboscopic schlieren, point-diffraction interferometry, and laser-doppler velocimetry, flow information could be acquired which revealed hitherto unknown features about the flow reversal/separation onset processes, the influence of compressibility, and the mechanism of flow reattachment. The application of state-of-the-art Navier-Stokes computations showed their ability to correctly predict certain global trends, such as the dependence of lift and pitching moment on pitch rate, Mach number, and leading-edge geometry during the upstroke, but that they are deficient to model the detailed dynamic stall onset and the dynamic flow reattachment features.

It is felt that the experimental techniques are sufficiently well in hand to proceed from the study of the basic dynamic stall flow physics to the investigation of promising dynamic stall delay and control concepts because the successful implementation of such concepts will critically depend on the detailed visualization and measurement of the flow sensitivity to small changes in airfoil geometry, especially near the leading-edge. Efforts along these lines are planned for the near future.

Acknowledgements

The authors gratefully acknowledge the support of the following organizations and individuals:
NASA Ames Research Center, Dr. S. Davis;
U.S. Army Research Office, Fluid Mechanics Division, Dr. T. Doligalski;
U.S. Air Force Office of Scientific Research, Aerospace Sciences Division, Capt. H. Helin, Maj. D. Fant;
U.S. Naval Air Systems Command, Research and Technology Directorate, Mr. T. Momiyama.

References

1. Carr, L.W., J.Aircraft Vol.25, No.1, Jan 1988, pp. 6-17
2. Carr, L.W., Platzer, M.F., Chandrasekhara, M.S., Ekaterinaris, J.A., Numerical and Physical Aspects of Aerodynamic Flows, IV (T.Cebeci Ed.), 239-256 (Springer Verlag 1990)
3. Chandrasekhara, M.S. and Carr, L.W., J.Aircraft, Vo.27, No.6, June 1990, pp. 516-522
4. Chandrasekhara, M.S. and Brydges, B.E., AIAA-90-0575 (1990)
5. Chandrasekhara, M.S. and Carr, L.W., AIAA-90-3038 (1990)
6. Carr, L.W., Chandrasekhara, M.S., Ahmed, S., Brock, N.J., AIAA-91-0007 (1991)
7. Carr, L.W., Chandrasekhara, M.S., Brock, N.J., AIAA-91-1683 (1991)
8. Chandrasekhara, M.S. and Ahmed, S., AIAA-91-1799 (1991)
9. Ahmed, S. and Chandrasekhara, M.S., AIAA-91-3225 (1991)
10. Grohsmeier, S.P., Ekaterinaris, J.A., Platzer, M.F., AIAA-91-1798 (1991)
11. Clarkson, J.D., Ekaterinaris, J.A., Platzer, M.F., 6th Int. Symp. Unsteady Aerodynamics, Aeroacoustics and Aeroelasticity University of Notre Dame, Indiana, 15-19 Sept. 1991
12. Carta, F.O. and Lorber, P.F., J. Propulsion, Vol.3, No.2, pp. 164-170, 1987
13. Hancock, G.J. and Mabey, D.G., AGARD-CP-465, Paper No. 14, 1989
14. Cebeci, T. Carr, L.W., Jang, H.M., AIAA-89-0020 (1990)
15. Walker, G.J., Subroto, P.H., Platzer, M.F., ASME-88-GT-32, 1988
16. Cebeci, T., Carr, L.W., Jang, H.M., AIAA-89-0020
17. Cebeci, T., Platzer, M.F., Chen, H.H., Jang, H.M., to be published

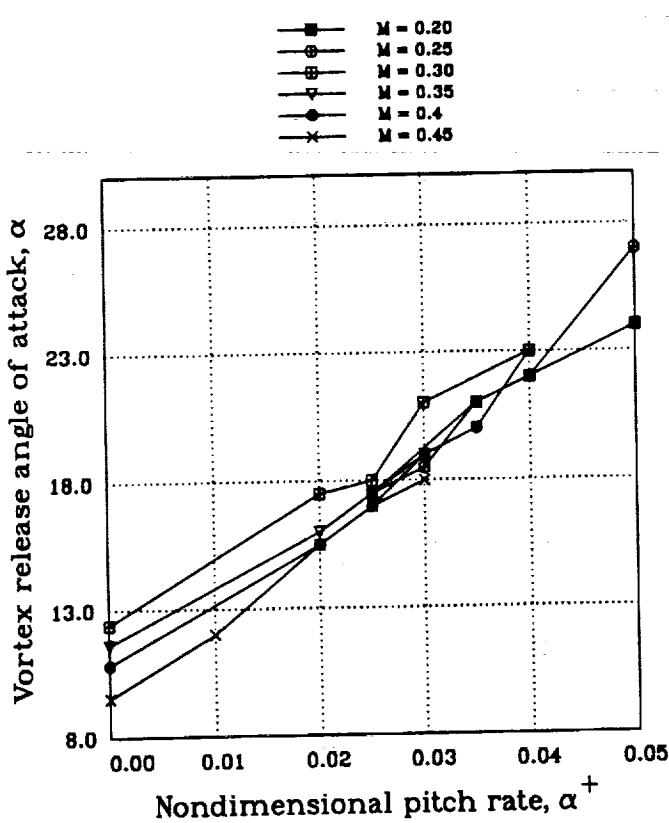


Fig. 1a Effects of Compressibility and Unsteadiness on Dynamic Stall Angle for a Transiently Pitching Airfoil

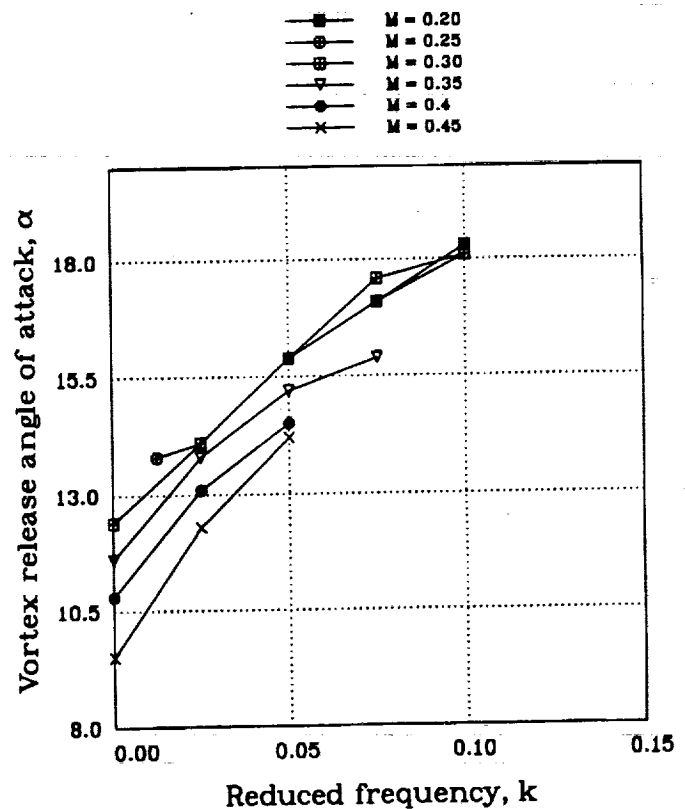


Fig. 1b Effects of Compressibility and Unsteadiness on Dynamic Stall Angle for an Oscillating Airfoil



Fig. 2 Schlieren Picture of Multiple Shocks on Rapidly Pitching NACA 0012 Airfoil

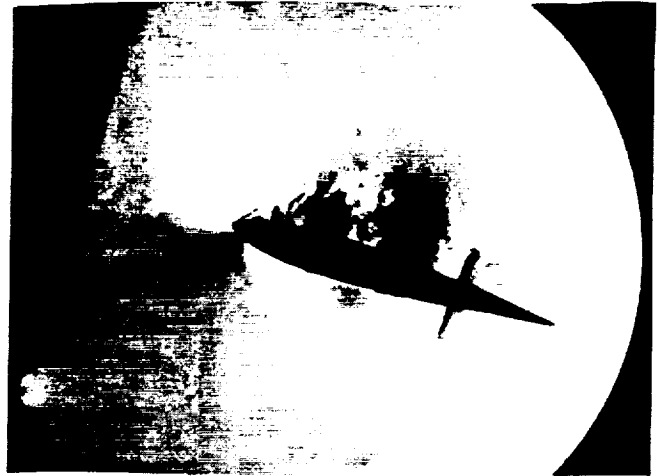


Fig. 3 Multiple Vortices on Rapidly Pitching NACA 0012 Airfoil



Fig. 4a Point Diffraction Interferogram of Oscillating NACA 0012 Airfoil
AOA=10 degrees, $M=0.33$, $k=0.075$

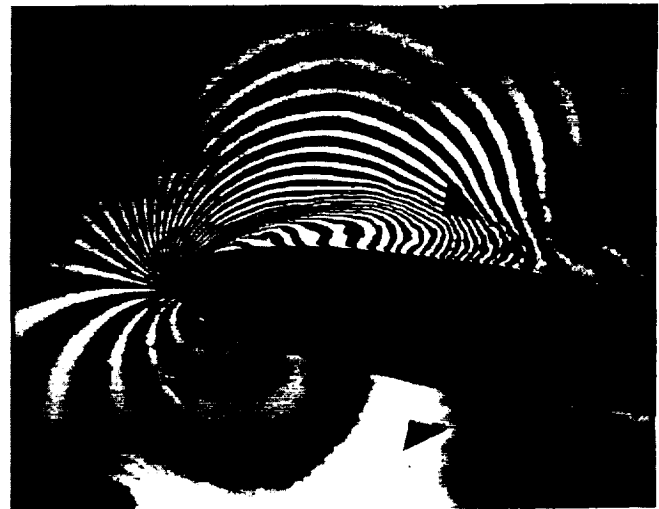


Fig. 4b Point Diffraction Interferogram of Oscillating NACA 0012 Airfoil
AOA=13.6 degrees, $M=0.33$, $k=0.075$

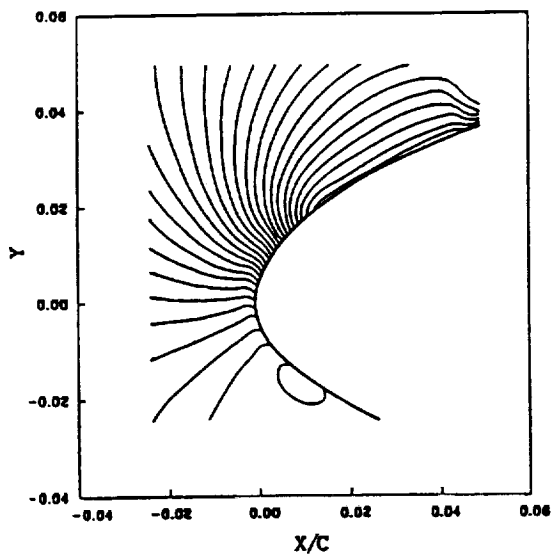


Fig. 5a Fringe Contours Near Leading Edge of Steady NACA 0012 Airfoil
AOA=10 degrees, $M=0.3$, $k=0$

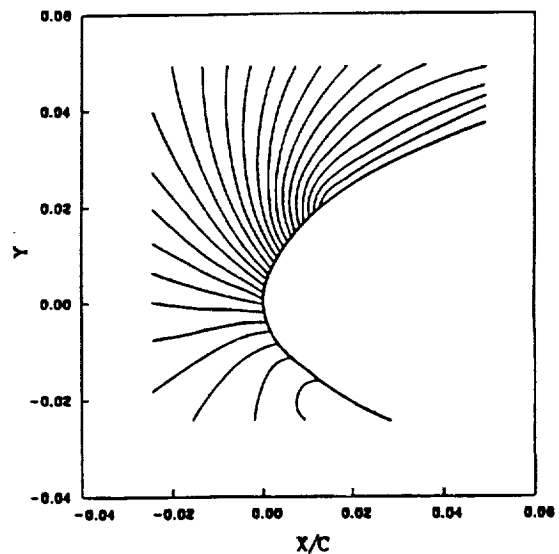


Fig. 5b Fringe Contours Near Leading Edge of Oscillating NACA 0012 Airfoil
AOA=10 degrees, $M=0.3$, $k=0.1$

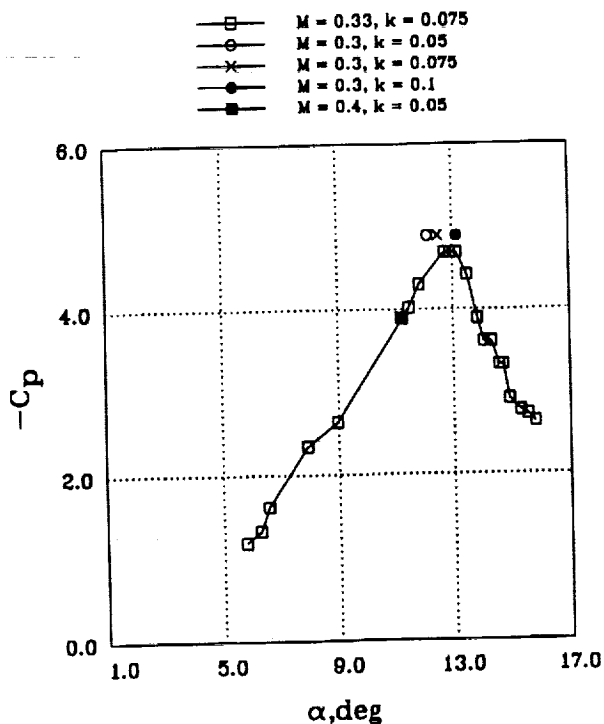


Fig. 6 Minimum Pressure Coefficient as Function of Angle of Attack at Various Mach Numbers, as Determined from PDI Interferograms

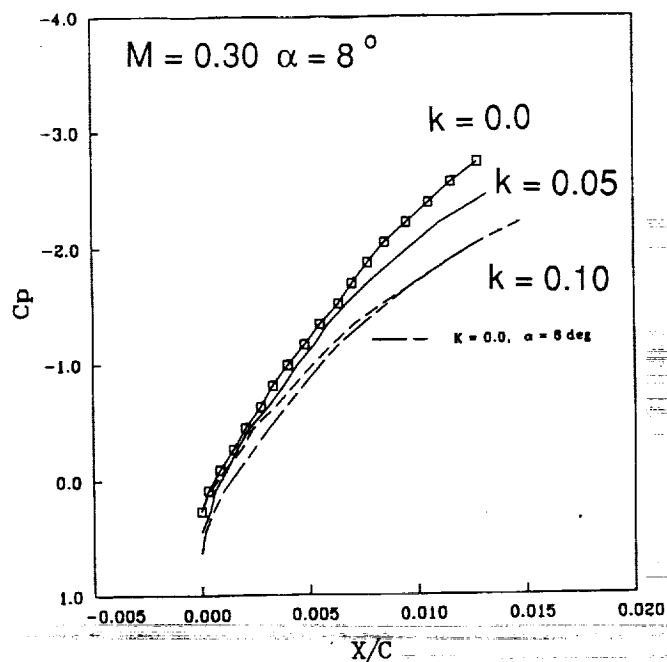


Fig. 7 Pressure Distributions for Several Reduced Frequencies for NACA 0012 Airfoil as Determined from PDI Interferograms
M = 0.3, AOA = 8 degrees

PHASE DISTRIBUTION OF U at X/C = 0.083
(ORIGIN SHIFTED BY 0.20 AT EACH Y/C)

Δ	Y/C = 0.200	⊠	Y/C = 0.117
+	Y/C = 0.183	×	Y/C = 0.100
x	Y/C = 0.167	◆	Y/C = 0.083
◇	Y/C = 0.150	⊙	Y/C = 0.067
▽	Y/C = 0.133		

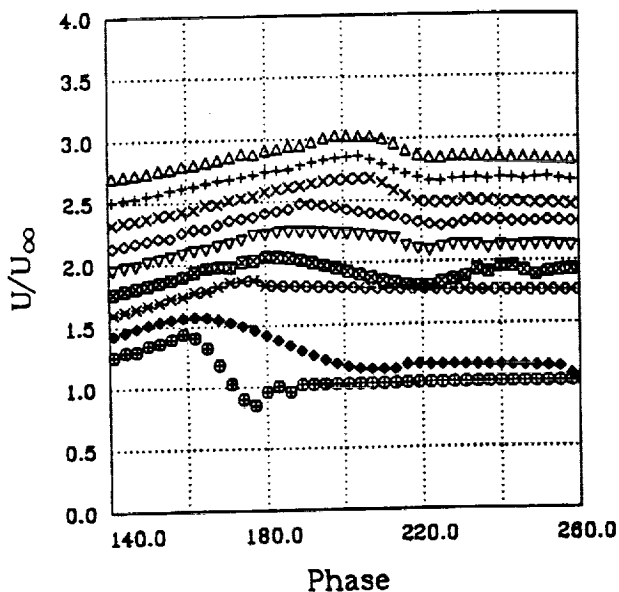


Fig. 8a U-Component Measurements in the Separation Bubble, x/c = 0.083

PHASE DISTRIBUTION OF V at X/C = 0.083
(ORIGIN SHIFTED BY 0.20 AT EACH Y/C)

○	Y/C = 0.300	▽	Y/C = 0.133
Δ	Y/C = 0.200	⊠	Y/C = 0.117
+	Y/C = 0.183	×	Y/C = 0.100
x	Y/C = 0.167	◆	Y/C = 0.083
◇	Y/C = 0.150	⊙	Y/C = 0.067

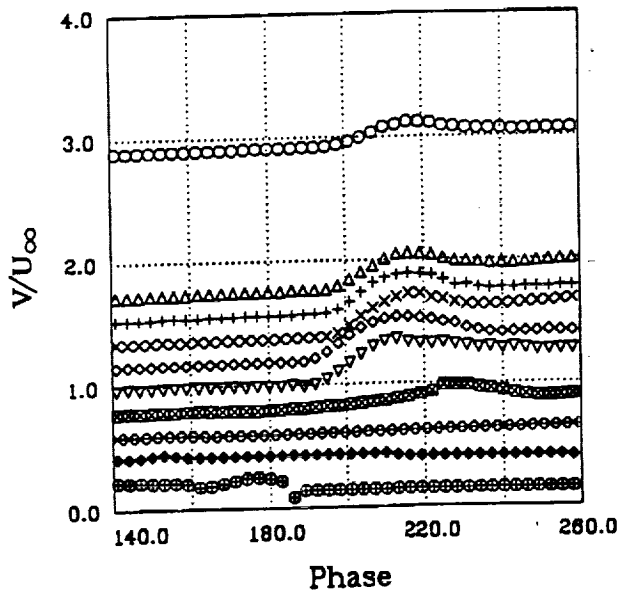


Fig. 8b V-Component Measurements in the Separation Bubble, x/c = 0.083

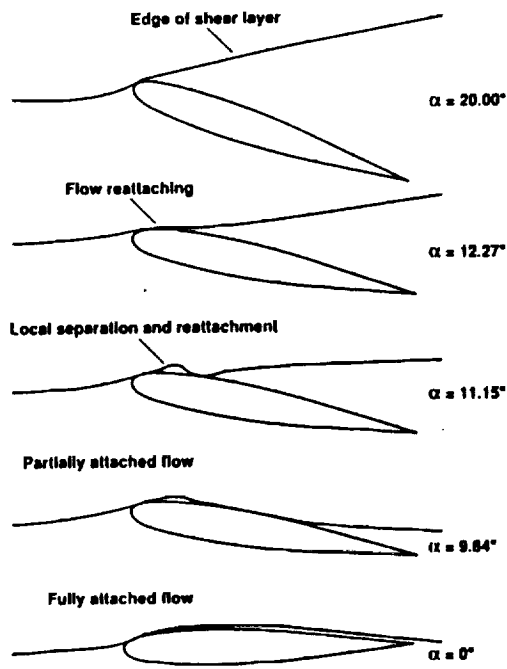


Fig. 9 Schematic of the Reattachment Process

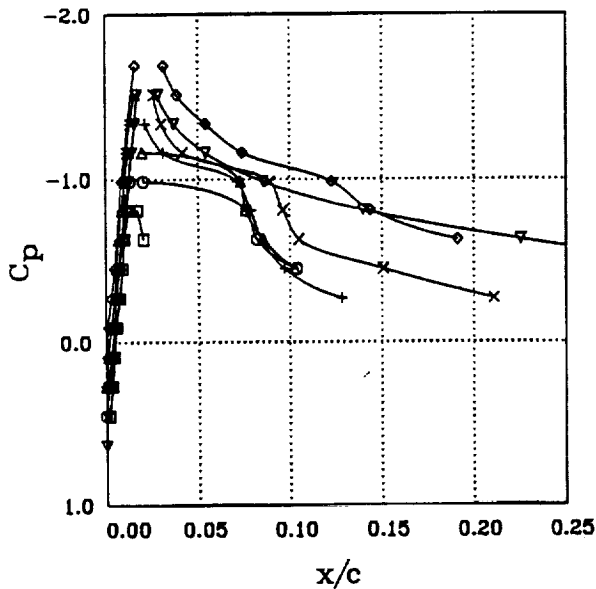


Fig. 11 Pressure Distribution during Reattachment

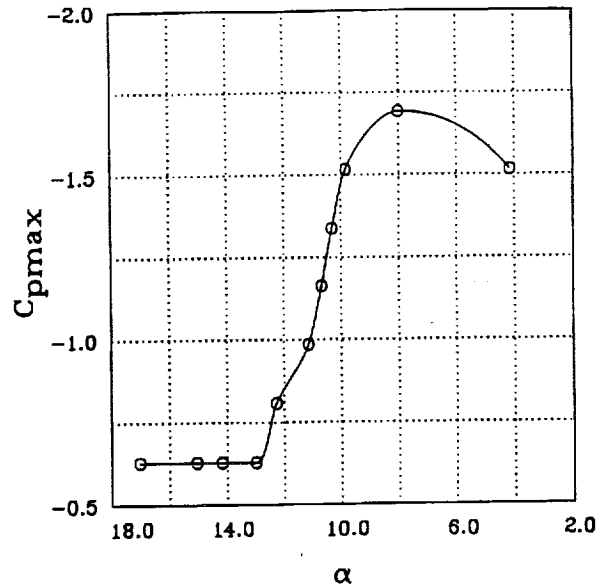
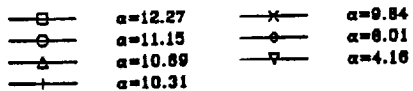


Fig. 10 Variation of Maximum Suction Pressure

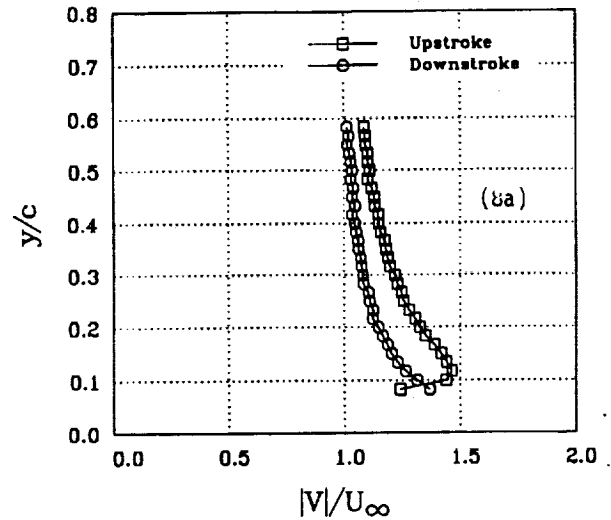


Fig. 12a Comparison of Velocity Magnitudes at AOA = 10 degrees

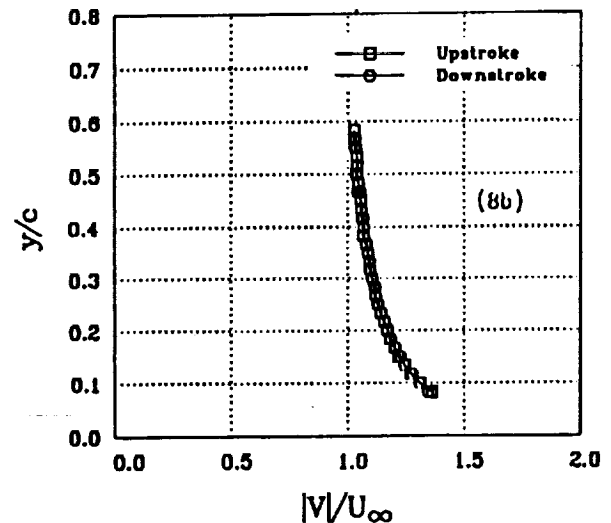


Fig. 12b Comparison of Velocity Magnitudes at AOA = 5.46 degrees

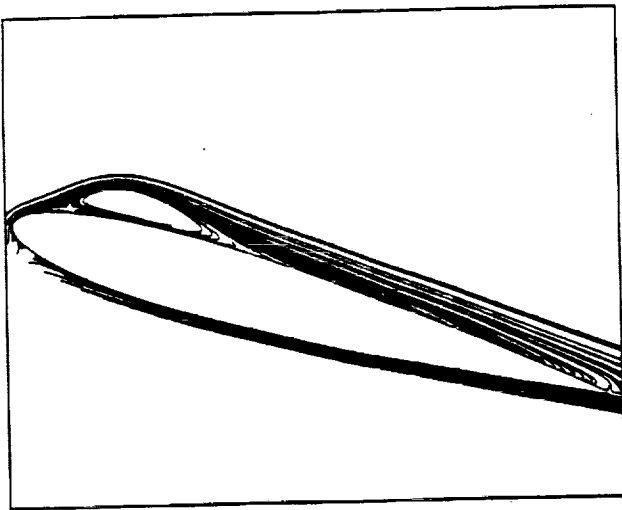


Fig. 13 Computed Flow Field on NACA 0012 Airfoil Pitching Upward at a Rate of 0.02 through AOA = 17 degrees, M = 0.4, Re = 4 million

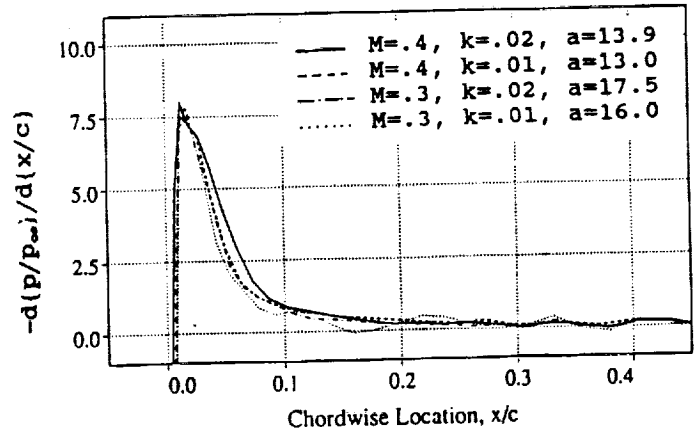


Fig. 14 Computed Pressure Gradient Distributions at the Onset of Flow Reversal on NACA 0012 Airfoil

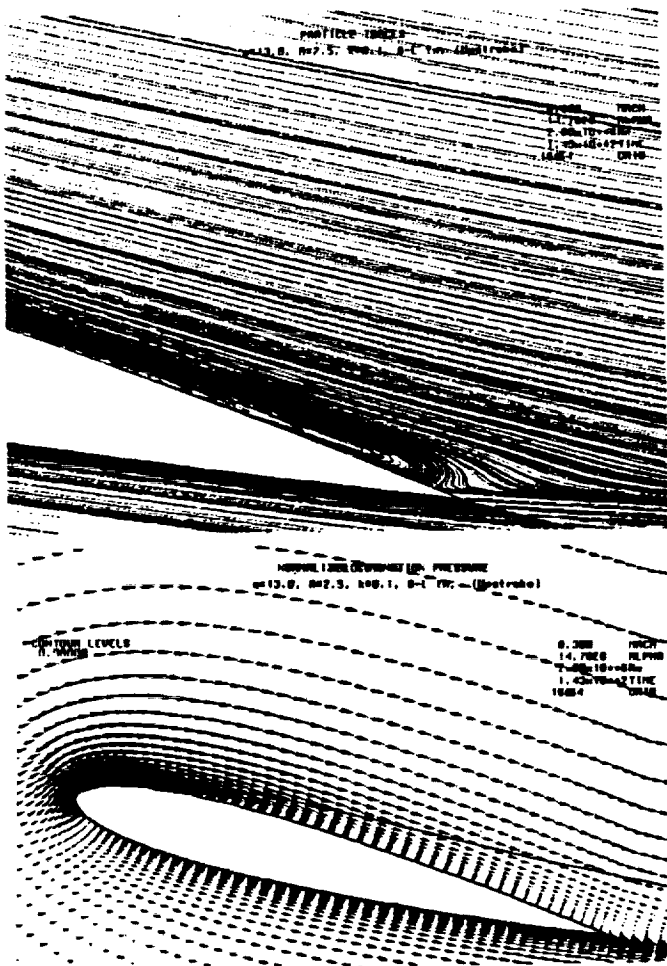


Fig. 15 Computed NACA 0012 Flowfield during Upstroke, AOA=14.7 degrees M=0.3, k=0.1, Re = 2 million

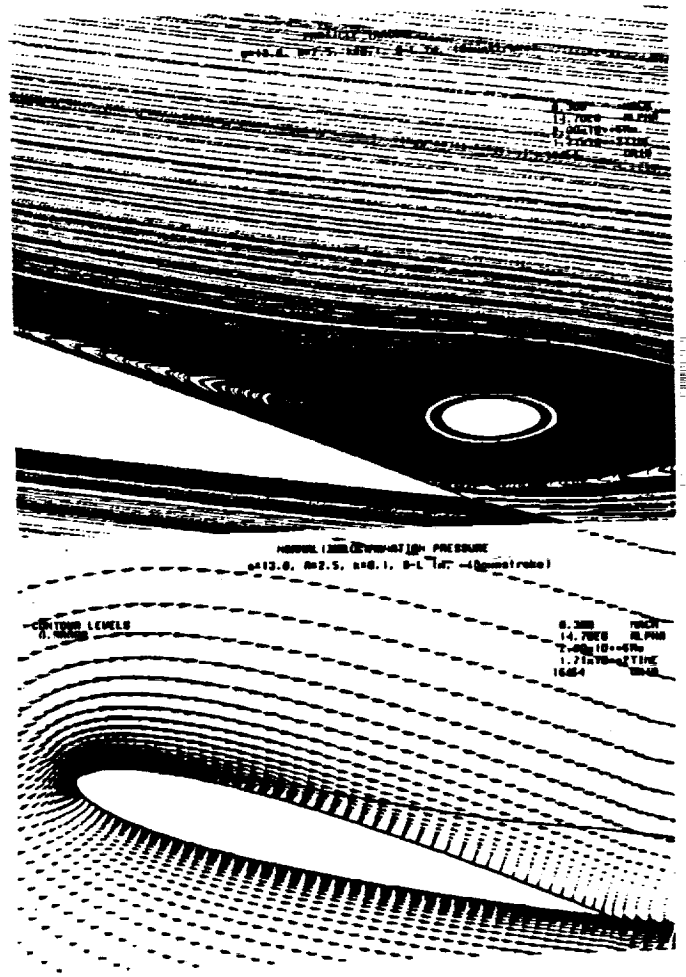


Fig. 16 Computed NACA 0012 Flowfield during Downstroke, AOA=14.7 degrees M=0.3, k=0.1, Re = 2 million

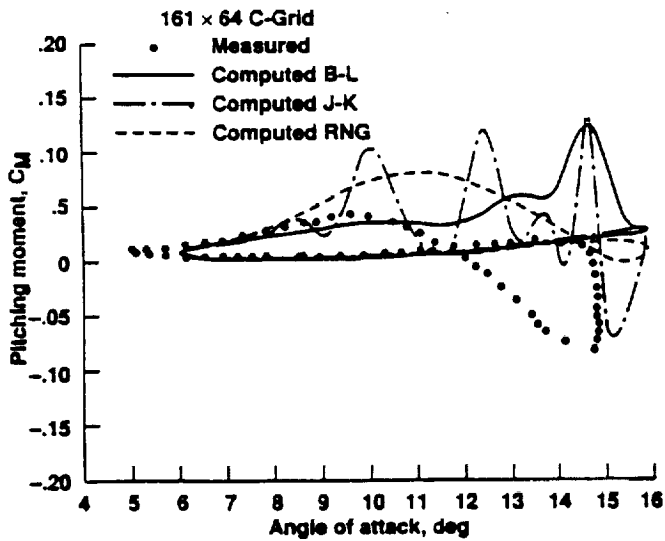


Fig. 17 Computed and Measured Pitching Moment Hysteresis on NACA 0012 Airfoil

$M_\infty = 0.3$, $\alpha(t) = 11^\circ + 5^\circ \sin(\omega t)$, $k = 0.1$, $Re = 4 \times 10^6$
Experiment: McCroskey

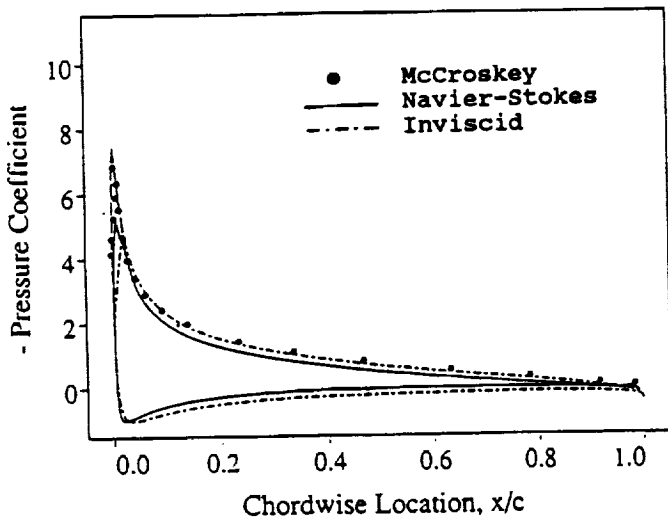


Fig. 18a Computed and Measured Pressures on NACA 0012 Airfoil during Upstroke at AOA = 11.9 degrees
 $M = 0.3$, $k = 0.2$, $Re = 4$ million

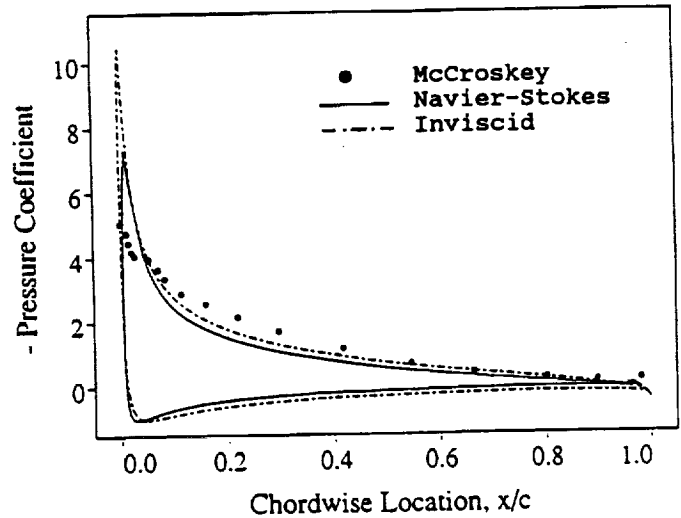


Fig. 18b Computed and Measured Pressures on NACA 0012 Airfoil during Downstroke at AOA = 13.7 degrees
 $M = 0.3$, $k = 0.2$, $Re = 4$ million

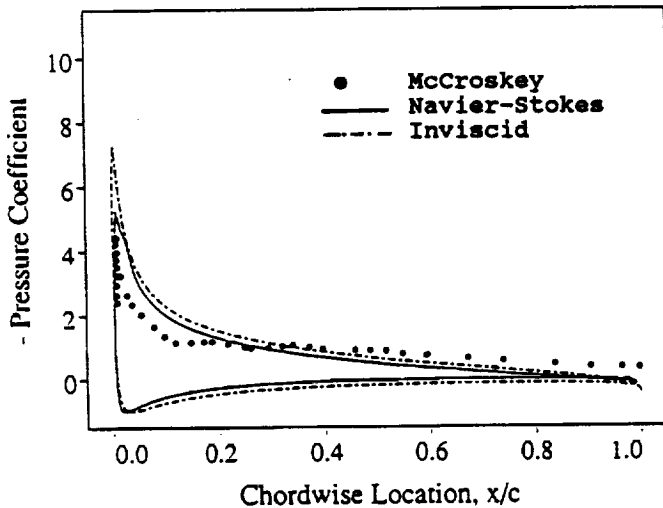


Fig. 18c Computed and Measured Pressures on NACA 0012 Airfoil during Downstroke at AOA = 10.5 degrees
 $M = 0.3$, $k = 0.2$, $Re = 4$ million

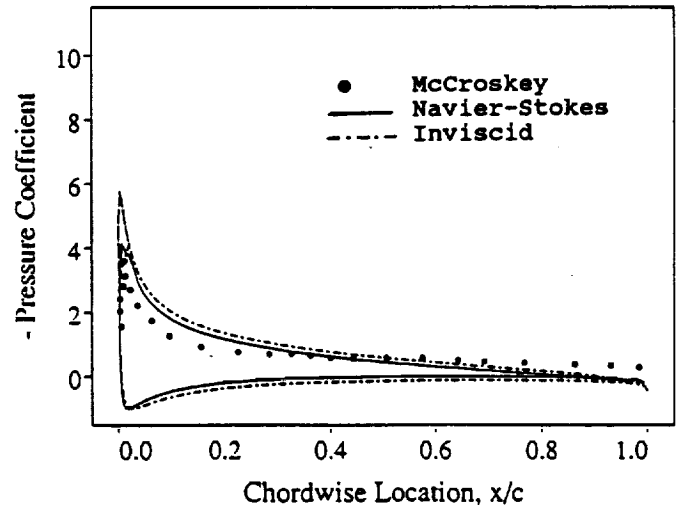


Fig. 18d Computed and Measured Pressures on NACA 0012 Airfoil during Downstroke at AOA = 8.9 degrees
 $M = 0.3$, $k = 0.2$, $Re = 4$ million

